Molecular dynamics study of the interactions between dislocation and imperfect stacking fault tetrahedron in Cu

Lucie Saintoyant [a,b], Hyon-Jee Lee [b], Brian D. Wirth [b,*]

[a] *Institut National Polytechnique de Grenoble, ENSPG, France*
[b] *Department of Nuclear Engineering, University of California Berkeley,*
MC 1730, Berkeley, CA 94720-1730, USA

Abstract

The microstructure of irradiated face centered cubic alloys with low stacking fault energy is distinguished by the formation of a high number density of nanometer size stacking fault tetrahedra (SFT). A recent transmission electron microscopy investigation of high-energy proton irradiated copper [16] has shown that nearly 50% of the visible SFT population are not perfect SFTs, but rather consist of truncated SFT and/or groups of overlapping SFT. This paper presents the results of atomistic molecular dynamics simulations of the interaction between gliding dislocations, of either edge or screw character, and truncated SFT or overlapping SFT. The most common result of the edge dislocation interaction with a truncated SFT is defect shearing, ultimately leading to complete separation into two smaller defect clusters. Partial absorption of the truncated SFT is the most common result of the interaction with a screw dislocation, resulting in the formation of super-jog (or helical) segments as the defect is absorbed into the dislocation core. The resulting non-planar screw dislocation is self-pinned with reduced mobility and is re-emitted as a similar truncated SFT as the applied shear stress is increased. The re-emitted truncated SFT is often rotated and translated relative to the original position. These observations are consistent with the hypothesis that shearing (decreased defect cluster size) and dislocation dragging of the defect clusters by partial absorption into the dislocation core contributes to the formation of defect-free channels.
© 2006 Elsevier B.V. All rights reserved.

1. Introduction

Performance degradation of structural steels in nuclear environments may limit the extended operation of light-water nuclear reactors and restrict the design of advanced fission and fusion reactors [1–3]. The qualitative aspects of micro-structural evolution and mechanical property changes are reasonably well established for neutron or high-energy particle irradiation in copper alloys [4–15], and are generic to most metals. However, quantitative and predictive models of constitutive property changes, as well as a complete fundamental understanding of the underlying microstructure–property relationships, controlling degradation are lacking.

Irradiation of copper at low to intermediate homologous temperatures ($T < \sim 0.5\ T_m$) causes an increase in yield and ultimate strength, a decrease

* Corresponding author. Tel.: +1 510 642 5341; fax: +1 510 643 9685.
E-mail address: bdwirth@nuc.berkeley.edu (B.D. Wirth).

in ductility, a decrease in the work hardening rate, and at higher irradiation levels, the appearance of a well-defined initial yield point and subsequent yield drop [4,5,7,10,11,14,15]. The microstructure of Cu following neutron or high-energy particle irradiation has been extensively characterized by transmission electron microscopy (TEM) [8,9,11–15] and generally consists of a high number density of nanometer-sized defects. The dominant irradiation induced defects in copper are stacking fault tetrahedra (SFT), Frank partial and perfect dislocation loops, and a mixture of bubbles and voids that evolve at higher doses [8,9,11–15]. In Cu, the SFT number density increases linearly with dose until reaching a saturation density of $\sim 10^{24}$ m^{-3} [13], while the mean SFT size observed in TEM studies is roughly constant at about 2.5 nm over a wide temperature range [12,13]. More recent TEM observations of high-energy proton irradiated Cu single crystals by Schaublin et al. indicate that nearly 50% of the visible SFT population does not consist of perfect SFTs, but rather are truncated SFT and/or groups of overlapping SFT [16].

Following deformation of irradiated metals, TEM examination of the microstructure frequently reveals the existence of localized deformation in the form of 'defect-free channels'. The channels, which appear free of irradiation induced defects, are generally on the order of 100 nm wide with a spacing of approximately 1 μm [7,8,13–15,17,18]. While a number of models have been proposed to describe the dislocation–defect interactions responsible for the removal of irradiation defects within the channels and the sequence of events leading to channel formation [7,8,19–21], neither the dislocation–defect interactions, the channel evolution, nor the correlation between the channels and the observed tensile stress–strain behavior are fully understood.

The atomistic interactions between gliding dislocations and perfect SFT have recently been studied using molecular dynamics (MD) simulations by many research groups [22–28]. These simulations show that the SFTs are a strong obstacle to motion and are generally sheared as a result of the interaction. The observed interactions between SFT and screw dislocations are more complex than for edge dislocations, due to the ability of the screw dislocation to cross-slip [24–28]. Partial absorption of the base portion of the SFT has been observed in some interactions [25–28], and this absorption does depend on the interaction geometry and dislocation velocity (e.g., applied stress or strain rate). However, neither complete absorption nor collapse of the perfect SFT has been observed, even after interaction with multiple dislocations. The MD simulations reported to date [22–28] have predominately investigated perfect SFTs, although Wirth et al. report that an overlapping truncated SFT is absorbed into the core of an edge dislocation, leading to the formation of super-jogs [22]. In that simulation, the resulting super-jog pair significantly reduced dislocation mobility and was subsequently re-emitted as a new and different defect cluster in an Orowan-type detachment process. The MD simulations are largely consistent with in-situ TEM straining experiments that have investigated dislocation–Frank loop interactions in irradiated copper [29] and dislocation–SFT interactions in quenched gold [30,31].

However, relatively little is known regarding the interaction of dislocations with truncated SFT or groups of overlapping SFT. Yet, as reported by Schaublin and co-workers, these defects account for nearly 50% of the SFT population [16]. Therefore, we have performed detailed MD studies of the interaction behaviour between edge or screw dislocations with truncated or overlapping SFTs as a function of their interaction geometry and applied stress. Section 2 describes the simulation method and Section 3 presents key observations from these MD simulations. Section 4 presents a discussion of the results, with an emphasis on comparing the observed interactions with truncated SFT and overlapping SFTs to those of perfect SFTs, and the implications for understanding the dislocation channel formation mechanism. Section 5 presents the conclusions of this study.

2. Simulation method

The MD simulations of the interaction of gliding dislocations, of either screw or edge type, and a truncated SFT in Cu were performed using the MDCASK code [32] and the Mishin embedded atom method (EAM) potential [33]. This potential is well adapted to the study of SFT-defects and interaction with partial dislocations of dissociated perfect dislocations, since both the stacking fault energy and the elastic constants are well fit to the experimental values.

All simulations were performed in a rectangular cell bounded by $(\bar{1}11)$, (110) and $(1\bar{1}2)$ planes.

Periodic boundary conditions were used in the $Y = \frac{1}{2}[110]$ and $Z = \frac{1}{2}[1\bar{1}2]$ directions, while the $X = [\bar{1}11]$ direction is a free surface on which a constant surface traction (force) is applied to provide a shear stress on the $(\bar{1}11)$ planes of the system. This cell geometry is identical to the previous work by Wirth et al. [22].

The screw dislocation simulations used a cell size of 12.5 nm in the X direction, 22.5 nm in the Y direction and 17.7 nm in the Z direction. To ensure the continuity of the (110) plane across the z boundary in the presence of a screw dislocation, the boundary condition is modified following the scheme introduced by Rodney [23]. The edge dislocation simulations used a cell size of 12.5 nm in the X direction, 18.4 nm in the Y direction and 23 nm in the Z direction. Thus, the SFT-defect density is $\sim 2.0 \times 10^{23}$ m^{-3} for both edge and screw simulations, and is comparable with the experimental results [12,13]. An edge dislocation was introduced in the simulation cell by removing two $(2\bar{2}0)$ half-planes. The dislocation density was $\sim 4.4 \times 10^{15}$ m^{-2} in simulations.

The dislocations and the defects are visualized by identifying atoms with HCP stacking and atoms which are neither HCP nor FCC stacking, using a common neighbour analysis method [34]. The HCP atoms are represented as light color circles in the figures, while the atoms in neither HCP nor FCC lattice are dark color circles. Vacancies are identified by the coordination number of nearest neighbor atoms. For example, a single vacancy is surrounded by 12 atoms, each of which has 11 nearest neighbor atoms.

Truncated or overlapping SFT are introduced by removing atoms on the {111} plane. The truncated SFT consisted of 98 vacancies in a trapezoidal shape, while the overlapping SFT consisted of 100 vacancies in a diamond shape. Fig. 1 shows the structure of these two SFT-defects. The truncated SFT can be formed either from the dislocation reactions associated with the dissociation of the Frank partial loop (as formed here), or from the complete shear of a perfect SFT into two smaller defects through dislocation interactions. Thus, the truncated base portion of a sheared SFT is consistent with the truncated SFT formed through dissociation of a trapezoidal shaped Frank loop, as observed in Lee et al. [28].

All simulations were performed at an initial temperature of 100 K. During equilibration, the dislocation, $b = \frac{1}{2}[110](\bar{1}11)$, naturally dissociates into two Shockley partial dislocations $\left(\frac{1}{6}[12\bar{1}] + \frac{1}{6}[211]\right)$ separated by a stacking fault. The mean separation distance was 2.2 nm and 4.4 nm for the screw and edge dislocation at 100 K, respectively. After 20 ps of equilibration, a shear stress of 100 MPa was
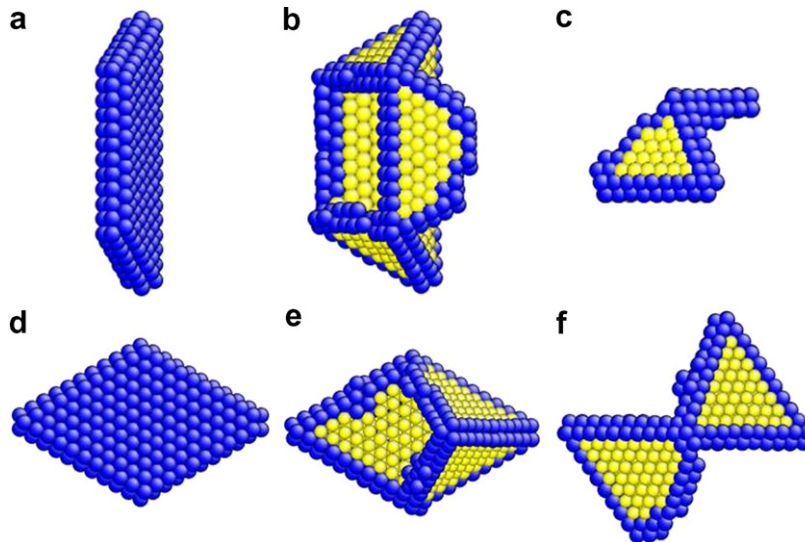

Fig. 1. Snapshots from MD simulations showing the structure of truncated SFT and overlapping SFT. The truncated SFT is formed from a trapezoidal shaped vacancy platelet on the $(1\bar{1}1)$ plane, (a) initial structure in $[\bar{1}11]$ projection, (b) final structure in $[\bar{1}11]$ projection, (c) final structure in $[110]$ projection. The overlapping SFT is formed from a diamond shaped vacancy platelet, (d) initial structure in $[\bar{1}11]$ projection, (e) final in $[\bar{1}11]$ projection, (f) final structure in $[110]$ projection. In this and all following figures, the atoms in HCP stacking are shown as yellow (light) circles and the atoms in neither FCC nor HCP stacking are shown as blue (dark) circles. (For interpretation of the references in colour in this figure legend, the reader is referred to the web version of this article.)

applied and the dislocation–defect interaction was visualized. If strong dislocation pinning was observed, as defined by no indication of pending dislocation detachment during 20 ps of applied stress, then the applied shear stress was increased in 100 MPa increments.

3. Results

3.1. Truncated SFT

A series of simulations using different interaction geometry have been performed to study the interaction of an edge or screw dislocation with a truncated SFT. In all simulations, the truncated platelet of vacancies was introduced on the $(11\bar{1})$ plane with a dislocation glide plane of $(\bar{1}11)$. The configuration of the truncated SFT is shown in Fig. 1(a)–(c) and the results are summarized in Table 1. Specific examples are discussed in more detail below.

3.1.1. Screw dislocation
3.1.1.1. Equilibrium defect structure without applied shear stress. The 98 vacancy platelet was positioned immediately next to the screw dislocation. The screw dislocation rapidly dissociates into two partials and the vacancy platelet forms a truncated SFT during the equilibration at 100 K. By changing the position of screw dislocation on the $(\bar{1}11)$ glide plane with respect to the vacancy platelet, as summarized in Table 1, different interaction geometries were investigated. However, the results observed were similar for all of the MD simulations.
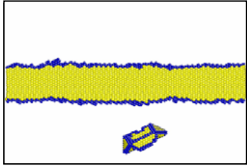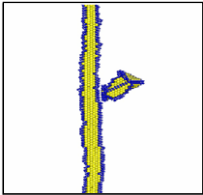
Fig. 2 shows a series of MD simulation snapshots of the interaction between a screw dislocation, which lies on the base plane of the vacancy platelet, and a truncated SFT, which formed from the vacancy platelet (in $[1\bar{1}2]$ projection). Fig. 2(a) shows the initial configuration of the screw dislocation on the base plane of the truncated SFT. During the first few picoseconds at 100 K, the screw dislocation dissociates into two Shockley partial dislocations and a truncated SFT forms from the vacancy platelet. During the first two picoseconds (Fig. 2(b)), the dislocation interacts with and partially absorbs the defect. The interaction leads to a configuration in which the dislocation is bounded by a defect composed of three stair-rod and three Shockley partial dislocations as shown in Fig. 2(c). Note, that following the definition in standard dislocation text books [35], the stair-rod dislocations are lines in the $\langle 110 \rangle$ direction where two stacking faults on $\{111\}$ planes meet. The configura-

tion continues to evolve and by 10 ps, the dislocation has essentially completely absorbed the truncated SFT, with cross-slipped and climbed segments of the screw dislocation connected by super-jog-type segments (or alternately, individual segments associated with a helical turn on the screw dislocation) (Fig. 2(d)). Over longer times, the dislocation configuration is observed to fluctuate between two different states. One configuration consists of partial defect absorption, with a smaller SFT-like defect clearly identifiable in the dislocation core (as shown in Fig. 2(c) and (e)). The other configuration involves complete defect absorption (Fig. 2(d)) into the dislocation core. Thus, the resulting dislocation configuration without an applied shear stress following interaction with the truncated SFT consists of a line segment (s) which has cross-slipped (partial absorption) and an additional segment that has climbed (complete absorption) with super-jogs (helical segments) caused by the partial or complete absorption of the truncated SFT.

3.1.1.2. Defect structure following dislocation detachment with an applied shear stress. MD simulations have also been performed with an increasing applied shear stress, starting from interaction geometries similar to that of Fig. 2, to investigate the critical shear stress for detachment, the interaction and detachment mechanism, and the resulting defect structure. Fig. 3 shows a series of MD simulation snapshots (in $[\bar{1}11]$ projection) of the interaction under an incrementally increasing applied shear stress. Fig. 3(a) shows the dislocation–defect configuration after 40 ps at 100 K with no applied a stress. Fig. 3(b)–(d) show configurations with a shear stress of 100 MPa. Fig. 3(e) and (f) show the configuration with a stress of 200 MPa and Fig. 3(g) and (h) are at an applied stress of 300 MPa. The 100, 200 and 300 MPa shear stresses were applied for 30, 20 ps and 20 ps, respectively. Initially, the dislocation remains pinned by the super-jogs (or helical turn), even with the application of an applied shear stress, as shown in Fig. 2(d), although the super-jog segments fluctuate (migrate) along the dislocation line. After the application of a shear stress of 300 Mpa for about 3 ps, the dislocation finally detaches from the defect cluster (Fig. 3(h) and (i)). The resulting defect is still a truncated SFT, which has rotated 60° compared to the initial position and been moved about 12 nm along the dislocation line. Thus, despite absorption of the truncated SFT, the dislocation ultimately detaches from the defect under an applied

Table 1
Summary of the observed interactions between a truncated SFT and an edge or a screw dislocation for different interaction geometries relative to the dislocation glide plane

	Edge dislocation	Screw dislocation
Top of the Truncated SFT	Dislocation bypass leaves the defect unchanged	Super-jog pair (helical turn)
One layer under the top of the truncated SFT	2 vacancies are removed	One vacancy is removed. The dislocation leaves the defect in the same configuration
Two layer under the top of the truncated SFT	Dislocation pinned	5 vacancies are removed and the dislocation is pinned by an helical turn
Middle of the Truncated SFT	Dislocation pinned	Super-jog pair (helical turn)
One layer above the base of the truncated SFT	Partial absorption and re-emission, resulting in removal of about 15 vacancies after multiple dislocation interactions, and rotation of the re-emitted defect cluster	2 vacancies are removed and the dislocation is pinned by an helical turn
Base of the Truncated SFT	Dislocation bypass leaves the defect unchanged	Super-jog pair (helical turn)
Under the truncated SFT	Dislocation bypass leaves the defect unchanged	Dislocation bypass leaves the defect unchanged

shear stress, and leaves behind the same truncated SFT-defect structure as initially encountered.

3.1.2. Edge dislocation

An example of an edge dislocation interaction with the truncated SFT is presented in Fig. 4. This particular interaction geometry had the dislocation glide plane situated one layer above the base plane of the truncated SFT (in $[\bar{1}11]$ projection). The MD simulation was performed with a constant applied shear stress of 100 MPa, rather than an incrementally increasing stress. Following application of the shear stress, the dislocation glides

towards the defect (Fig. 4(a)) and after 12 ps, begins to interact. At 15 ps, the dislocation passes the (1 1 1) face of the defect (Fig. 4(b)). Later, as the leading partial passes the $(1\,1\,\bar{1})$ face of the defect, the stacking fault on this face is removed, while a new stacking fault is formed on the $(1\,\bar{1}\,1)$ face (Fig. 4(c) and (d)). The dislocation then detaches from the truncated SFT about 30–35 ps after applying a 100 MPa shear stress. Consequently, as shown in Fig. 4(e) and (f), the final configuration of the truncated SFT is similar, but is again rotated relative to the original configuration. As well, and perhaps more importantly, the passage of the
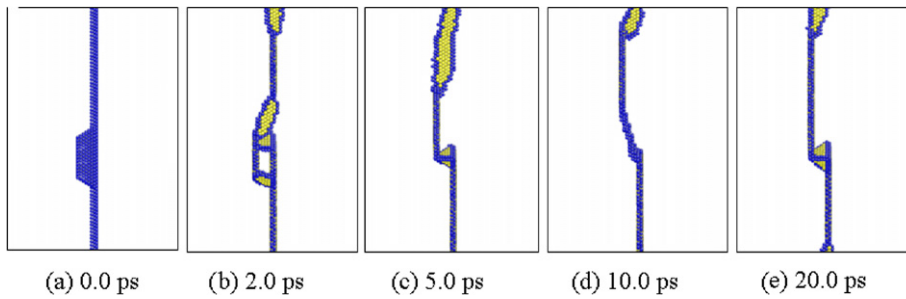
(a) 0.0 ps   (b) 2.0 ps   (c) 5.0 ps   (d) 10.0 ps   (e) 20.0 ps

Fig. 2. Snapshots in time and [1 1̄ 2] projection from an MD simulation at 100 K, showing the interaction of a screw dislocation and a truncated SFT without an applied shear stress.
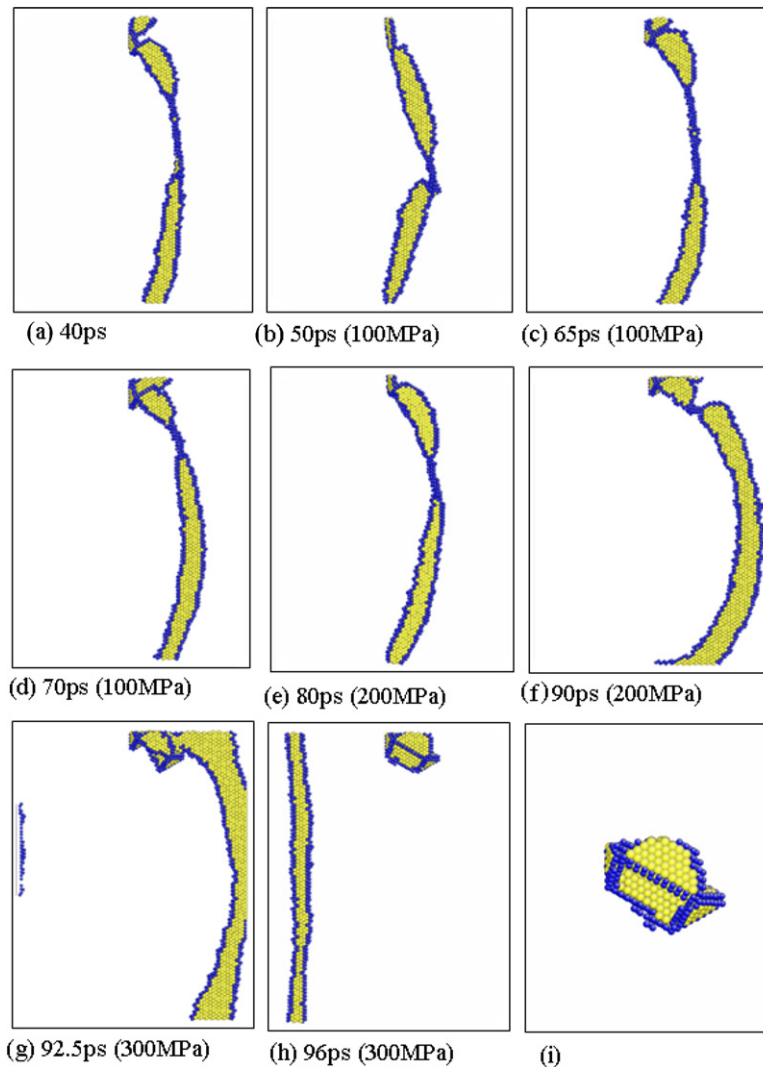

(a) 40ps   (b) 50ps (100MPa)   (c) 65ps (100MPa)

(d) 70ps (100MPa)   (e) 80ps (200MPa)   (f) 90ps (200MPa)

(g) 92.5ps (300MPa)   (h) 96ps (300MPa)   (i)

Fig. 3. Snapshots in time and [1̄ 1 1] projection from an MD simulation at 100 K, showing the sequence of events during the interaction of a screw dislocation and a truncated SFT with an applied shear stress. (a) Configuration of the partially absorbed defect cluster and screw dislocation with a helical turn following 40 ps at 100 K without applied stress. Observed evolution with an applied shear stress of (b)–(d) 100 MPa and (e, f) 200 MPa (g), (h). Observed evolution at an applied stress of 300 MPa as the screw dislocation detaches and (i) the resulting defect structure.
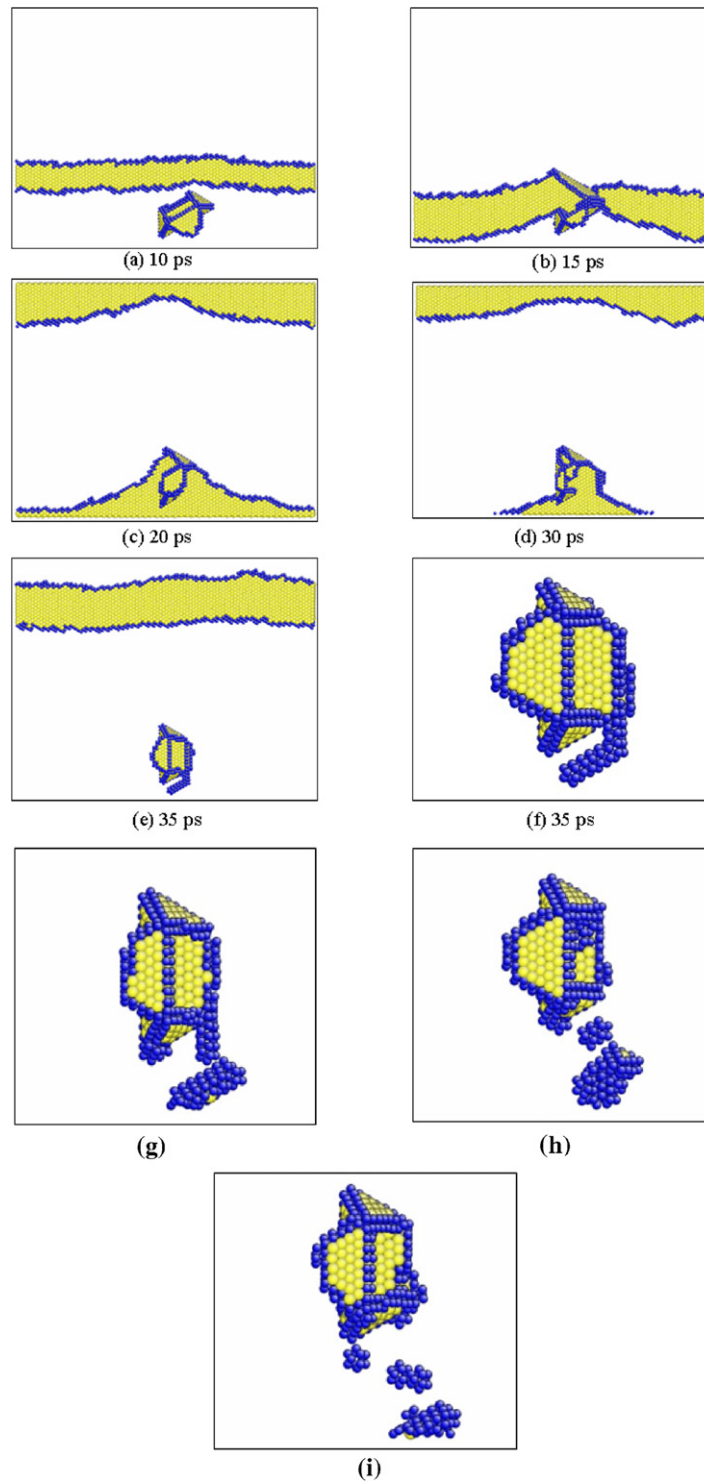
Fig. 4. Snapshots in time and $[\bar{1}11]$ projection from an MD simulation at 100 K, showing the interaction between a moving dissociated edge dislocation and a truncated SFT, whose base lies one layer under the glide plane of the dislocation. Dislocation positions are shown at (a) 10.0 ps, (b) 15.0 ps, (c) 20 ps, (d) 30 ps, (e) and (f) 35 ps after applying a 100 MPa shear stress, (g)–(i) showing the resulting structure after multiple dislocation interactions through the periodic boundary condition, (g), 3 shear interactions (h), 6 shear interactions and (i) 9 shear interactions.

dislocation has decreased the defect size, with the removal of seven vacancies. These seven vacancies were temporarily absorbed into the dislocation core during the interaction, and then re-deposited outside the truncated SFT as a row of vacancies. The resulting defect configuration, including the row of seven vacancies, is shown in more detail in Fig. 4(f).

This MD simulation was continued to observe multiple interactions between the edge dislocation and defect cluster as the dislocation passed through the periodic boundary condition. Fig. 4(g)–(i) show the truncated SFT configuration following the 3rd, 6th and 9th dislocation interaction and bypass, respectively. Notably, the truncated SFT is slightly reduced in size with each shear interaction. The final configuration simulated actually consists of a number of isolated vacancies, a small vacancy cluster and a truncated SFT that contains approximately 81 rather than 98 vacancies.

When the dislocation glides on the mid-plane between the base and top portion of the truncated SFT as shown in Fig. 5, the results are more sensitive to the specific interaction geometry. Configurations associated with initially placing the truncated vacancy platelet on either the $(11\bar{1})$ plane or the (111) plane have been investigated. Fig. 5(a) and (c) shows the configuration of the truncated SFT on either the $(11\bar{1})$ or the (111) plane following

20 ps at 100 K without applied stress, respectively. At this time, a 100 MPa shear stress is applied and the dislocation begins to move toward the defect structure. When the initial vacancy platelet is on the $(11\bar{1})$ plane (Fig. 5(a)), the edge dislocation is strongly pinned (blocked) by the defect as shown in Fig. 5(b). The dislocation remains pinned as the applied stress is increased up to 500 MPa, with an increment of 100 MPa per 20 ps. On the other hand, when the initial vacancy platelet is on the (111) plane, as shown in Fig. 5(c), the dislocation partially absorbs the defect by forming super-jog segments and leaves a smaller defect and several small vacancy clusters behind (Fig. 5(d)). The result of the partial absorption of the truncated SFT by the edge dislocation is that the dislocation now has a reduced mobility associated with the super-jog pair, and the defect cluster has been broken down into two smaller vacancy defect clusters and an isolated vacancy.

3.2. Overlapping SFT

The overlapping SFT is formed from a 100 vacancy platelet with a diamond shape on the {111} plane, as shown in Fig. 1(d)–(f). During equilibration, the vacancy platelet rapidly forms two nearly perfect SFTs, one above and one below the initial {111} plane, as shown in Fig. 1(e) and (f).
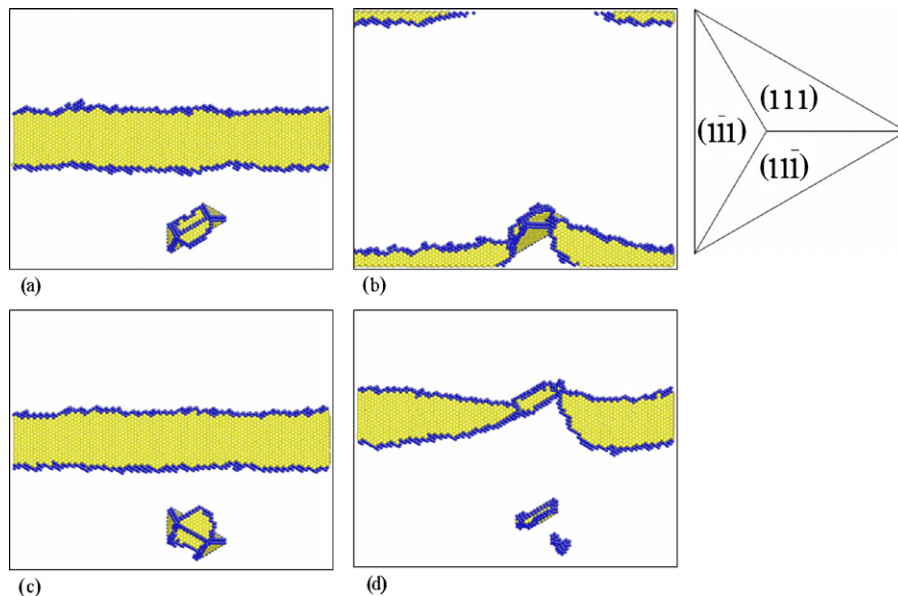

Fig. 5. Snapshots in time and $[\bar{1}11]$ projection from an MD simulation at 100 K, showing the interaction of an edge dislocation and a truncated SFT in different configurations under a 100 MPa shear stress. (a) and (c) show the initial configuration. Figure (b) and (d) show the configuration after applying a shear stress. On the right, schematic $[\bar{1}11]$ projection of the tetrahedron of Thomson is showing the different planes.

3.2.1. Screw dislocation

Fig. 6 shows MD simulation snapshots (in [$\bar{1}$11] projection) of the resulting structure following interaction of the screw dislocation with the overlapping SFT. For the interaction geometry shown in Fig. 6(a), the dislocation initially interacts with only one stair-rod partial of the overlapping SFT structure, partially absorbing the overlapping SFT as evidenced by the removal of stacking faults shown in Fig. 6(b). The result of this interaction is that the entire screw dislocation has cross-slipped onto an alternate glide plane and remains strongly pinned, as shown in Fig. 6(b).

On the other hand, no partial absorption or cross-slip is observed when the screw dislocation initially contacts the overlapping SFT at the corner of one SFT where three stair-rod dislocations intersect, as in the interaction geometry shown in Fig. 6(c). No cross-slip is observed during this interaction, and the dislocation is able to shear the defect, bypassing at a critical stress less than 100 MPa. As a result of the shear interaction, a pair of ledges is introduced on the overlapping SFT as shown in Fig. 6(d). The ledges consist of an intrinsic and extrinsic surface step, consistent with the ledge structure observed in the shear of an isolated perfect SFT.

3.2.2. Edge dislocation

Fig. 7 shows a series of MD simulation snapshots (in [$\bar{1}$11] projection) of the interaction between an edge dislocation and an overlapping SFT whose base plane lies on the dislocation glide plane. Initially a shear stress of 100 MPa is applied and within 20–25 ps, the dislocation absorbs the defect as shown in Fig. 7(a)–(d). The resulting structure of the dislocation from the (partial) absorption of the overlapping SFTs is quite complicated and consists of a super-jog pair and a climbed segment of the edge dislocation, in addition to smaller portions of the initial overlapping SFT which are not absorbed into the dislocation core, as shown in Fig. 7(d). This structure persists and pins the edge dislocation at applied shear stresses of 100 and 200 MPa. Upon
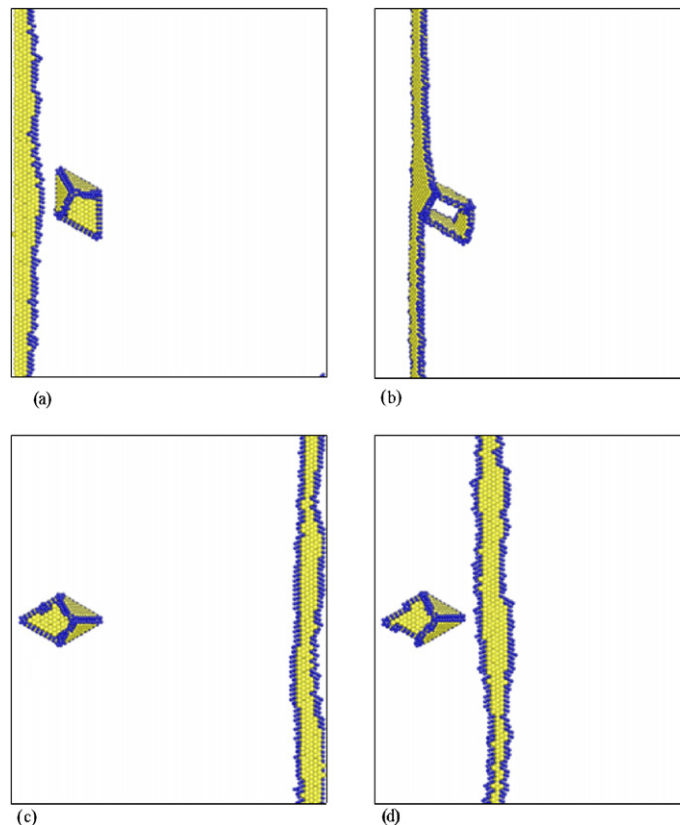

Fig. 6. Snapshots in time and [$\bar{1}$11] projection from an MD simulation at 100 K, showing the initial (a) and (c) and final (b) and (c) configuration of the interaction between a screw dislocation and an overlapping SFT, for different interaction configuration.
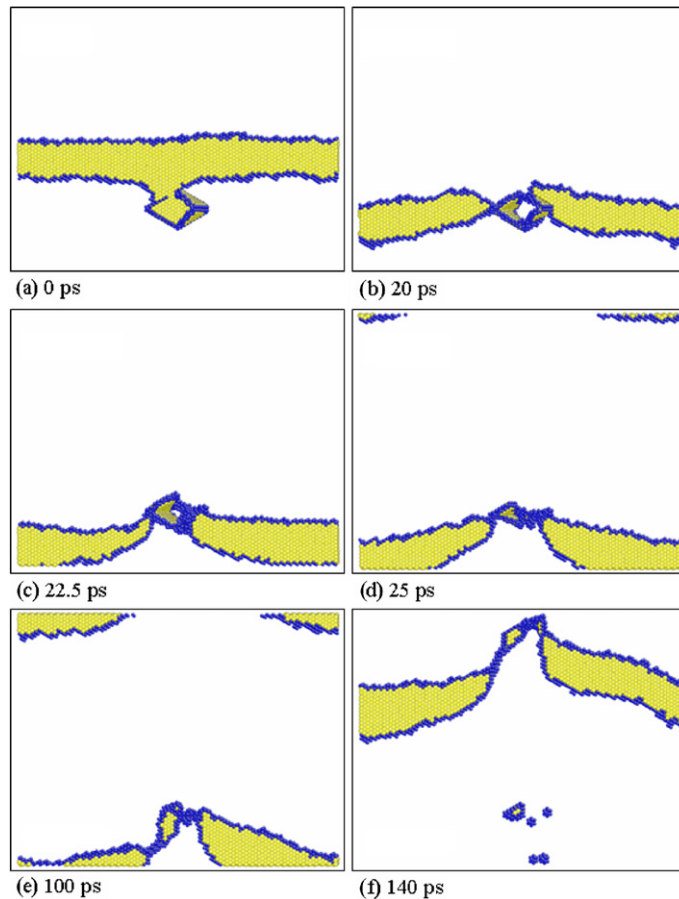
Fig. 7. Snapshots in time and $[\bar{1}11]$ projection of an MD simulation at 100 K, showing the evolution of the interaction of an overlapping SFT and an edge dislocation under a progressive shear stress. During the first 20 ps, a shear stress of 100 MPa is applied (a)–(d), during the next 20 ps 200 MPa was applied, and then 300 MPa is applied during 20 ps. Finally the dislocation unpins (e) and (f) when a 400 MPa shear stress is applied.

applying a 300 MPa shear stress, the dislocation begins to drag the super-jog and defect structure, as shown in Fig. 7(e). Upon further increasing the applied shear stress to 400 MPa, the dislocation is able to detach from this complex defect structure and migrate with a super-jog pair and a segment of dislocation that has climbed onto a neighbouring, parallel $(\bar{1}11)$ glide plane. Detachment involves the emission of multiple defects, including several isolated vacancies, one or more small vacancy clusters and a much smaller (compared to the initial 100 vacancies) faulted defect cluster.

4. Discussion

The present paper has shown that a screw dislocation, due to its ability to cross-slip, is efficient in absorbing, or partially absorbing the truncated

SFT. The partial or complete absorption of the truncated SFT results in a non-planar screw dislocation, containing super-jogs (or individual cross-slipped segments of a helical turn) that connect segments of dissociated screw dislocation on different {111} glide planes, as a result of cross-slip and/or climb processes. Pinning of the edge dislocation by the truncated SFT, or dislocation bypass without change in defect structure, was the most common observed result, although partial absorption of the truncated SFT by an edge dislocation was observed when the edge dislocation glide plane was one plane above or at the mid-plane location of the truncated SFT formed on the (111) plane.

The interaction between the screw dislocation and overlapping SFT also depends on the interaction geometry and can result in either shearing or screw dislocation cross-slip with partial absorption.

While more configurations remain to be investigated, it is notable that partial absorption of this defect did not produce a helical turn, but rather led to cross-slip of the full dislocation line with a dislocation 'lock' at the defect. The interaction between the edge dislocation and overlapping SFT resulted in the partial absorption of the overlapping SFT, with a decreased vacancy–defect cluster and some isolated vacancies remaining.

Thus, truncated and overlapping SFT are observed to be very strong obstacles to dislocation motion, as was the case of perfect SFT [22–28]. Indeed, screw dislocation glide is considerably slowed upon (partial) absorption of the defect as a result of self-pinning by the super-jog (helical turn) segments formed, and the edge dislocation was found to require an applied shear stress in excess of 500 MPa to bypass a truncated SFT formed on the $(11\bar{1})$ plane. Thus, partial to complete defect absorption always resulted in super-jog pair formation on the edge dislocation and a helical-like structure on the screw dislocation, which decreased the dislocation mobility (self-pinned the dislocations). At higher applied stresses, the screw dislocation always de-pinned from the super-jog, or helical turn, segments. The de-pinning process emitted a similar truncated SFT to that initially absorbed; although in many cases, the defect was rotated and dragged from its initial position. Additionally, the truncated SFT was reduced in size with the additional emission of one or more single vacancies.

The edge dislocation mobility was also significantly reduced by the presence of a super-jog pair for the configurations investigated. However, the edge dislocation was not observed to de-pin from the super-jog pair, which is different from the screw interaction and the previous results of Wirth et al. [23]. It is plausible that the larger defect cluster size, approximately twice as large as the experimental observations of about 2.5 nm [12,13], results in a somewhat larger super-jog pair separation, leading to less self-pinning. This effect may be responsible for such differences, as well as the larger stacking fault energy ($\sim$45 mJ/m^2) of the Mishin EAM Cu potential [33] compared to the values of about $\sim$11 mJ/m^2 used in the work by Wirth et al. [22].

These observations lead to the conclusion that dislocation channel formation is much more complicated than defect absorption in a single interaction, and may result from a combination of (i) decreased defect cluster size due to shear, (ii) partial absorption leaving isolated vacancies and smaller defect clusters of presumably reduced obstacle resistance, and (iii) partial to complete absorption and the subsequent dragging and re-emission of defect clusters at a different location.

5. Conclusion

Molecular dynamics simulations of edge or screw dislocation interactions with truncated SFT and overlapping SFTs have been performed to determine the atomistic sequence of events controlling the interaction and detachment, and the resulting defect structures. The results indicate that a number of complex interaction mechanisms occur, although the most common interaction involves shear of the defect cluster, especially when the dislocation has edge character. Partial to complete absorption of a truncated SFT is observed when the dislocation is of screw character, although absorption results in a non-planar dislocation structure consisting of super-jogs (or, alternately helical turn segments) connecting regions of the cross-slipped or climbed screw dislocation. The resulting non-planar screw dislocation has reduced mobility due to self-pinning, and is observed to re-emit a similar truncated SFT structure with increasing applied shear stress, although the defect is often rotated and transported from its original position. Partial absorption and shear also often results in removal of isolated vacancies from the defect, thereby breaking the truncated SFT or overlapping SFT into two or more smaller defect clusters.

These results are consistent with MD observations of dislocation interaction with perfect SFT and lead to the conclusion that the result of dislocation reaction with SFT, truncated SFT and overlapping SFT are largely governed by shear interactions, producing smaller defects, with partial absorption possible for specific interaction geometries. Partial absorption is much more likely for screw dislocations due to the ability of the screw dislocation to cross-slip. However, even for partial absorption, defect re-emission is the most likely result, unless thermally activated diffusion processes, which are inaccessible to MD modeling, can transport the super-jog pair (helical turn segments) away from the absorption and thereby reduce the pinning strength. These observations are also consistent with the idea that the dislocation channels are most likely the consequence of multiple dislocation–defect interactions, in which the defect cluster size is decreased and some of the defects are dragged

and re-emitted through partial absorption events, rather than the collapse and complete annihilation or absorption of the SFT-defects.

Acknowledgements

References

[1] E.E. Bloom, J. Nucl. Mater. 258–263 (1998) 7.
[2] S.J. Zinkle, N.M. Ghoniem, Fusion Eng. Des. 51–52 (2000) 55.
[3] G.R. Odette, G.E. Lucas, JOM 53 (7) (2001) 18.
[4] A. Seeger, Proceedings of the 2nd UN International Conference on Peaceful Uses of Atomic Energy (Geneva, United Nations), 6 (1958) 250.
[5] T.H. Blewitt, R.R. Coltman, R.E. Jamison, J.K. Redman, J. Nucl. Mater. 2 (1960) 277.
[6] M.J. Makin, J.V. Sharp, Phys. Stat. Sol. 9 (1965) 109.
[7] J.V. Sharp, Acta Metall. 22 (1974) 449.
[8] E. Johnson, P.B. Hirsch, Philos. Mag. A 43 (1981) 157.
[9] C.A. English, B.L. Eyre, J.W. Muncie, Philos. Mag. A 56 (1987) 453.
[10] Y. Dai, D. Gavillet, F. Paschoud, M. Victoria, J. Nucl. Mater. 212–215 (1994) 393.
[11] B.N. Singh, A. Horsewell, P. Toft, D.J. Edwards, J. Nucl. Mater. 224 (1995) 131.
[12] S.J. Zinkle, L.L. Snead, J. Nucl. Mater. 225 (1995) 123.
[13] S.J. Zinkle, B.N. Singh, J. Nucl. Mater. 283–287 (2000) 306.
[14] M. Victoria, N. Baluc, C. Bailat, Y. Dai, M.I. Luppo, R. Schaublin, B.N. Singh, J. Nucl. Mater. 276 (2000) 14.
[15] B.N. Singh, D.J. Edwards, P. Toft, J. Nucl. Mater. 299 (2001) 205.
[16] R. Schaüblin, Z. Yao, N. Baluc, M. Victoria, Philos. Mag. 85 (2005) 769.
[17] I.G. Greenfield, H.G.F. Wilsdorf, J. Appl. Phys. 32 (1961) 827.
[18] J.L. Brimhall, B. Mastel, Appl. Phys. Lett. 9 (1966) 127.
[19] B.N. Singh, A.J.E. Foreman, H. Trinkaus, J. Nucl. Mater. 249 (1997) 103.
[20] T. Diaz de la Rubia, H. Zbib, T.A. Khraishi, B.D. Wirth, M. Victoria, M.J. Caturla, Nature 406 (2000) 871.
[21] N.M. Ghoniem, S.H. Tong, B.N. Singh, L.Z. Sun, Philos. Mag. A 81 (2001) 2743.
[22] B.D. Wirth, V.V. Bulatov, T. Diaz de la Rubia, J. Eng. Mater. Tech. 124 (2002) 329.
[23] D. Rodney, Acta Mater. 52 (2004) 607.
[24] Y.N. Osetsky, R.E. Stoller, Y. Matsukawa, J. Nucl. Mater. 329–333 (2004) 1228.
[25] D. Rodney, Nucl. Instrum. and Meth. B 228 (2005) 100.
[26] Y.N. Osetsky, R.E. Stoller, D. Rodney, D.J. Bacon, Mater Sci. Eng. A 400 (2005) 370.
[27] P. Szelesteyl, M. Patriarca, K. Kaski, Modelling Simul. Mater. Sci. Eng. 13 (2005) 541.
[28] H.-J. Lee, J.-H. Shim, B.D. Wirth, J. Mater. Res., submitted for publication.
[29] J.S. Robach, I.M. Robertson, B.D. Wirth, A. Arsenlis, Philos. Mag 83 (2004) 955.
[30] J.S. Robach, I.M. Robertson, H.-J. Lee, B.D. Wirth, Acta Mater. 54 (2006) 1679.
[31] Y. Matsukawa, S.J. Zinkle, J. Nucl. Mater. 329–333 (2004) 919.
[32] T. Diaz de la Rubia, M.J. Guinan, J. Nucl. Mater. 174 (1990) 151.
[33] Y. Mishin, D. Farkas, M. Mehl, D. Papaconstantopoulos, A. Voter, J. Kress, Phys. Rev. B 63 (2001) 224106.
[34] A.S. Clarke, H. Jonsson, Phys. Rev. E 47 (1993) 3975.
[35] J. Weertman, J. Weertman, Elementary Dislocation Theory, Oxford University, 1992.